CHAPTER II

FORMULATION AND NUMERICAL METHOD

The physical problem and the computational domain is sketched in Figure 2.1. We have a wall bounded region in the z direction and the domain is periodic in the x direction. The bubble has constant physical properties denoted by the subscript i and the ambient fluid has properties denoted by the subscript o. The surface tension varies along the interface. The top wall is hot and the bottom wall is cold, and initially, the temperature is linearly increasing in the z direction.

2.1 Governing Equations

The Navier-Stokes equations are valid for both fluids, and a single set of equations can be written for the whole domain as long as the jump in viscosity and density is correctly accounted for and surface tension is included. The Navier-Stokes equations, in conservative form are as follows:

$$\frac{\partial \rho \mathbf{u}}{\partial t} + \nabla(\rho \mathbf{u}\mathbf{u}) = -\nabla p + \nabla \cdot \mu(\nabla \mathbf{u} + \nabla \mathbf{u}^T) + \int_B \delta(\mathbf{x} - \mathbf{x}_f)(\sigma \kappa \mathbf{n} + \frac{\partial \sigma}{\partial s}\mathbf{t})\, ds \tag{2.1}$$

In the last term, we include the surface tension forces acting on the interface as a body force by representing it as a delta function. Here, $\mathbf{u}$ is the velocity field, ρ is

the density, p is the pressure, μ is the viscosity, σ is the surface tension, κ is the mean curvature, $\mathbf{n}$ is a unit normal vector, $\mathbf{t}$ is a unit tangent vector, δ is the delta function, $\mathbf{x}_f$ is the position of the interface and the integral is over the interface separating the fluids.

The energy equation can be written as follows:

$$\rho c_p \left(\frac{\partial T}{\partial t} + \nabla \cdot (\mathbf{u}T) \right) = \nabla \cdot (k \nabla T), \tag{2.2}$$

where T is the temperature and k and c_p are the coefficients of heat conduction and heat capacity, respectively. Both fluids are immiscible and the physical properties are constant in each fluid. Therefore, the equations of state for density, viscosity, heat capacity and heat conduction can be written as follows;

$$\frac{D\rho}{Dt} = 0; \qquad \frac{D\mu}{Dt} = 0 \tag{2.3}$$

$$\frac{Dk}{Dt} = 0; \qquad \frac{Dc_p}{Dt} = 0. \tag{2.4}$$

The incompressibility constraint gives the divergence free velocity field condition as follows;

$$\nabla \cdot \mathbf{u} = 0. \tag{2.5}$$

If we combine the momentum equation and the incompressibility condition, this leads to a non-separable elliptic equation for the pressure. Since the physical properties are taken to be constant, the density field is independent of temperature variation and we have therefore excluded natural convection in this problem.

We take the surface tension to be a linearly decreasing function of the temperature:

$$\sigma = \sigma_o + \sigma_T (T_o - T) \tag{2.6}$$

where

$$\sigma_T = -(d\sigma/dT) = \text{constant}$$

and σ_o is the surface tension at a reference temperature T_o. In many cases, σ_T can be assumed to be a constant and for simplicity we assumed that it is so here. σ_T is positive for most fluids (see Braun *et al.* 1993 for negative value of σ_T). Therefore, increasing temperature reduces the surface tension. In a nonuniform temperature gradient, the cold side of the bubble will have a higher surface tension than the warm side and it will therefore pull surface from the warm side, where surface will be generated, around the bubble to the cold end, where the surface will disappear. This movement of the surface, with its viscous drag upon the outer fluid, will pick up a sheet of liquid and jet it off the cold back end. By jetting liquid one way, the bubble propels itself up the temperature gradient. Thermodynamically, such a self-propelling bubble is a heat engine. Whenever surface is created, heat is absorbed, and whenever surface is destroyed heat is given off. Therefore a swimming bubble absorbs heat at its hot end and rejects heat at its cold end (Trefethen, 1963).

2.2 Non-dimensional Numbers

Following other investigators we present our results in non-dimensional variables. The flow is governed by the following variables;

$$a,\ \sigma_o,\ \mu_o,\ \rho_o,\ c_{po},\ k_o,\ \mu_i,\ \rho_i,\ c_{pi},\ k_i,\ \sigma_T,\ \text{and}\ \nabla T_\infty.$$

Here a is a typical bubble or drop radius, σ_o is the average surface tension, μ is the viscosity, ρ is the density, c_p is the coefficient of heat capacity, k is the coefficient of heat conduction, σ_T is the rate of change of surface tension with temperature, and ∇T_∞ is the undisturbed temperature gradient in the ambient fluid far from the bubble. The physical properties of the bubble are denoted by the subscript i and those of the ambient fluid by the subscript o. This leads to the following

non-dimensional numbers;

$$\frac{\rho_i}{\rho_o},\ \frac{\mu_i}{\mu_o},\ \frac{c_{pi}}{c_{po}},\ \frac{k_i}{k_o},\ Ma = \frac{\sigma_T a^2}{\mu_o \alpha_o}\nabla T_\infty,$$

$$Re = \frac{\sigma_T \rho_o a^2}{\mu_o^2}\nabla T_\infty,\ \text{and}\ Ca = \frac{\sigma_T a}{\sigma_o}\nabla T_\infty$$

where,

$$\alpha_o = \frac{k_o}{\rho_o c_{po}}$$

Here, Ma is the Marangoni number, Re is the Reynolds number, and Ca is the average Capillary number. The average Capillary number is computed at the middle of the domain in the vertical direction. These three non-dimensional numbers are based on the properties of the outer fluid. Sometimes, the Prandtl number, $Pr_o = \nu_o/\alpha_o$, is used instead of the Re number. α_o is the thermal diffusivity of the outer fluid. As is usually done in the literature for Marangoni bubble motion, we define a reference velocity by:

$$U_r = \frac{\sigma_T a}{\mu_o}\ \nabla T_\infty.$$

The non-dimensional numbers can now be written in a much simpler form:

$$Ma = \frac{U_r a}{\alpha_o}, \qquad Re = \frac{U_r a}{\nu_o}, \qquad Ca = \frac{\mu_o U_r}{\sigma_o}$$

The Marangoni number is the Péclet number as it is usually used in the heat transfer literature and is the product of the Prandtl and the Reynolds number. When we present our results, velocities will be scaled by the reference velocity defined above and time will be scaled by the ratio of the initial bubble radius and the reference velocity. In the creeping flow regime, it is more appropriate to use diffusion time scale since the convection is negligible. Either viscous time scale or thermal time scale can be used. When the Prandtl number is very small than unity, the thermal field attains

its steady-state value while the fluid motion is just beginning to develop. Therefore, the flow is governed by the viscous time scale. When the Prandtl number is very large than unity, the fluid motion becomes quasi-static with a slowly-developing thermal field. Hence, the thermal time scale determines when the bubble reaches a steady state as pointed out by Dill (1988).

When the non-dimensional numbers are either small or large, several interesting limiting cases arise. At the zero Marangoni number limit, the energy equation reduces to the Laplace's equation for temperature since the convective transport of energy can be neglected in this case. Hence, the problem becomes a quasi-static problem. For a gas bubble, when the physical properties of the gas are much smaller than those of the ambient fluid, the energy transfer on the bubble surface can be neglected. This implies that the isotherms should be perpendicular to the bubble surface. Small Prandtl number results apply to liquid metals and large Prandtl number to heavy oils. Liquids have Prandtl numbers on the order of unity. Typical values are Pr=7 for water and Pr=0.72 for air, at standard conditions. The zero Reynolds number limit reduces the momentum equation to the steady case since inertial effects can be neglected in this limit.

When the Marangoni number is large, the convective terms in the energy equation are dominant. In this limit, conduction of energy can be neglected. If the Reynolds number is of the order of unity, large Prandtl numbers correspond to high Marangoni numbers. Heavy oils, like silicon oil, have large Prandtl numbers, on the order of 10^3.

In the limit of zero Capillary number, it can be assumed that deformation from a spherical shape is negligible. As the Capillary number increases, however, deformation of the bubble increases. If the deviation from a spherical shape is large,

the scaled terminal velocity of the bubble/drop decreases. In the zero Capillary, Marangoni and Reynolds number limit, the scaled migration velocity of a gas bubble is known to be 0.5.

In order to report the deformation of a bubble in later chapters, we define the deformation of a bubble as follows;

$$\gamma = \frac{1-\epsilon}{1+\epsilon}$$

where

$$\epsilon = \frac{\text{minor axis of the bubble}}{\text{major axis of the bubble}}.$$

In the simulations presented in this thesis, we include all terms in the governing equations and do not impose any restrictions inherent for these limiting cases.

2.3 Numerical Method

The numerical technique used for the simulations presented here is the Immersed Front Tracking method for multi-fluid flows developed by Unverdi (1990) and discussed by Unverdi and Tryggvason (1992 a,b). To solve the Navier-Stokes equations we use a fixed, regular, staggered grid and discretize the momentum equations using a conservative, second order centered difference scheme for the spatial variables and an explicit second order time integration method. We have used first order time integration in other problems and generally find little differences for the relatively short simulation times of interest here. The effect does show up in long time simulations, however, and is usually accompanied by a failure to conserve mass. In the computations discussed here, mass is always conserved within a fraction of a percent. The interface is represented by separate computational points that are moved by interpolating their velocity from the grid. These points are connected to form a front

that is used to keep the density and viscosity stratification sharp and to calculate surface tension forces. At each time step, information must be passed between the front and the stationary grid. This is done by a method that has become known as the Immersed Boundary Technique and is based on assigning the information carried by the front to the nearest grid points. While this replaces the sharp interface by a slightly smoother grid interface, all numerical diffusion is eliminated since the grid-field is reconstructed at each step.

The original Immersed Boundary Technique was developed by Peskin and collaborators (see e.g. Peskin (1977)) for homogeneous flows. The extension to stratified flows includes a number of additional complications. The first is that density now depends on the position of the interface and has to be updated at each time step. There are several ways to do this but we use a variant of the method developed by Unverdi (1990) where the density jump at the interface is distributed onto the fixed grid to generate a grid-density-gradient field. The divergence of this field is equal to the Laplacian of the density field and the resulting Poisson equation can be solved efficiently by a Fast Poisson Solver. The particular attraction of this method is that close interfaces can interact in a very natural way, since the grid-density gradients simply cancel. Therefore, when two interfaces come close together the full influence of the surface tension forces from both interfaces is included in the momentum equations, but the mass of the fluids in the thin layer between the interfaces—which is very small—is neglected. A second complication is that the pressure equation now has a nonconstant coefficient (or is non-separable) since the density varies. This prevents the use of Fast Poisson Solvers based on Fourier Methods, or variants there of. We used a simple SOR for many of our early computations (in the so-called Black and Red form for computations on a CRAY computer), but here, a multigrid

package (MUDPACK from NCAR) was used for most of the computations.

The computation of the surface tension forces poses yet another difficulty. Generally, curvature is very sensitive to minor irregularity in the interface shape and it is difficult to achieve accuracy and robustness at the same time. However, by computing the surface tension forces on each element directly by

$$F_s = \oint_{elem} \sigma \mathbf{n} \times \mathbf{t} ds, \tag{2.7}$$

we explicitly enforce that the integral over any portion of the surface gives the right value, and for closed surfaces, in particular, we enforce that the integral of surface tension forces is zero. This is important for long time simulations since even small errors can lead to a net force that moves the bubble in an unphysical way. Here, $\mathbf{n}$ is the surface normal vector, $\mathbf{t}$ is the unit vector tangent to the boundary of the surface element, σ is the surface tension coefficient.

The energy equation is solved in the same way as the momentum equation. Central differencing is used for the spatial derivatives on the staggered mesh and a second order time stepping is used to advance the temperature in time. The temperature on the front is interpolated from the neighboring stationary grid points by using an interpolation function invented by Peskin (1977). Given the temperature, surface tension can be found and the surface forces computed. The momentum and the energy equations are coupled through this relation.

We use different platforms to compute the simulations. This includes CRAY YMP and CRAY C90 supercomputers as well as HP, IBM RS/6000, IBM SP1 workstations. Due to the frequent crashes and the use of backup files in order to choose the low load times, it is hard to estimate the time to complete each run. It varies from one day to several days on a local workstation for two-dimensional simulations. This

goes as high as two months for three dimensional simulations on workstations.

2.4 Validation

In order to establish the correctness of the method presented here, we have done three tests to compare our results with existing analytical results. The first test is for the creeping flow regime. The terminal velocity of a single bubble rising in an unbounded domain has been found by Young *et al.* (1959). Young *et al.* utilize the solution of Hadamard and Rybczynski (1911) for flow around a fluid sphere and assume that convective transport of momentum and energy can be neglected. In other words, they assume that Reynolds and Marangoni numbers are very small and that the convective terms in the governing equations can be neglected. Once this is done, the problem becomes quasi-static. The energy equation reduces to a form where the Laplacian of temperature vanishes over the whole domain. They also assume that deformation from a spherical shape is negligible. This implies that Capillary effects can be neglected. They have given the scaled rising velocity as follows:

$$V_{YGB} = \frac{2}{(2+k^*)(2+3\mu^*)} \tag{2.8}$$

where k^* is the ratio of the coefficient of heat conductivity of the bubble to that of the ambient fluid and μ^* is the ratio of the viscosity of the bubble to that of the ambient fluid. For a gas bubble, since the conductivity and viscosity ratios are negligible, this formula reduces to $V_{YGB} = \frac{1}{2}$.

In an attempt to compare our results with the migration velocity of a bubble in the creeping flow regime, we first conducted resolution tests using two-dimensional simulations. The non-dimensional numbers are $Re = 2.5 \times 10^{-3}$, $Ma = 2.5 \times 10^{-3}$ and $Ca = 10^{-3}$ and the ratios of the physical properties of the bubble to that of

the outer fluid is 0.5. We have examined the sensitivity of the solution to the grid resolution by simulating a single bubble on 32×32, 64×64 and 128×128 grids for a square domain which extends four bubble radii in each direction. This corresponds to 16, 32 and 64 mesh points per bubble, respectively. As we increase the resolution the terminal velocities converge and the difference between the 64×64 grid and 128×128 grid is about 2%. Figure 2.2 shows the velocity versus time for these three runs.

We then do fully three dimensional simulations of a single bubble to compare our results with three-dimensional analytical solutions in the creeping flow regime. In order to reduce the computational costs, and due to limited computational resources, 32 grid points per bubble diameter were used in the three dimensional simulations. We have done these simulations for $Re = 2.5 \times 10^{-3}$, $Ma = 2.5 \times 10^{-3}$ and $Ca = 10^{-3}$. The ratios of the physical properties of the bubble to that of the outer fluid (k^* and μ^* in Equation (2.8)) are 0.5. The theoretical value of the rising velocity for a bubble migrating in an unbounded domain is 0.228 from Equation (2.8). Figure 2.3 shows the results of the fully three dimensional simulation of a single bubble migrating at steady state for these non-dimensional numbers. The migration velocity versus the distance, H, between the wall and the bubble centroid, scaled by bubble radius, is plotted in Figure 2.3. Since we have walls on the top and bottom of the computational domain as well as periodic horizontal boundaries, there are wall effects which reduce the rise velocity of the bubble. As we increase the size of the computational box, Figure 2.3 shows that the results approach the unbounded domain results.

For one of the cases in Figure 2.3, where the bubble is two bubble radii away from the wall, we plot the bubble and the temperature field in the middle plane of the computational box at steady state in Figure 2.4. The detailed structure of the

isotherms is shown in the middle plane in Figure 2.5. Figure 2.5 shows that the temperature field is consistent with the theoretical prediction that the temperature gradient inside the bubble does not change and the temperature field is uniform. For the same simulation, Figure 2.6 shows the velocity field in the middle cross sectional plane of the bubble while Figure 2.7 shows the detailed structure of this velocity field in the same plane.

In our second test we examine the qualitative behavior of a single bubble in the creeping flow regime with respect to changes in the ratio of the physical properties. Equation (2.8) indicates that the density and the heat capacity ratio do not play a role in the migration velocity of the bubble. The migration velocity is only affected by viscosity and heat conductivity according to Equation (2.8). Figure 2.8 shows the scaled migration velocity with respect to time for different viscosity ratios. When the bubble reaches steady state, it is seen clearly that beyond the viscosity ratio $\mu^* = 1/50$, the effect is negligible. This is consistent with Equation (2.8). While the viscosity ratio changes, the ratio of other physical properties are kept constant at unity. Similarly, the effect of the heat conductivity ratio is shown in Figure 2.9. While we decrease the ratio, we see that once it is smaller than about $k^* = 1/40$, the effect is negligible. Both of these results are qualitatively consistent with the prediction of Equation (2.8). We have also done a similar test for the density and heat capacity ratios. Figure 2.10 shows the effect of the density ratio while the effect of the heat capacity ratio is plotted in Figure 2.11. Both of these results show that these ratios do not change the migration velocity of the bubble at steady state as predicted by Equation (2.8). When the conductivity ratio is unity, the change in the heat capacity ratio does not change the energy equation. Therefore, in Figure 2.11, the test is done with the coefficient of heat conductivity ratio equal to 1/20. In all

these four different tests, the time is scaled by the viscous diffusion time scale. The other non-dimensional numbers are the same as for the three dimensional simulation, namely, $Re = 2.5 \times 10^{-3}$, $Ma = 2.5 \times 10^{-3}$ and $Ca = 10^{-3}$.

Finally, we show the results of a much simpler test. A strip of one fluid is laid down in a channel and surrounded by an ambient fluid. A schematic is shown in Figure 2.12. The domain is wall bounded in the vertical direction and periodic in the horizontal direction. There are two free surface at the top and the bottom of the symmetry axis x. The density of the middle layer is equal to the outer one, but its viscosity half of the outer one. We assume that the temperature field is fully developed and increases linearly with x. Since the surface tension is a function of temperature, the only force acting on each interface is the surface tension gradient along the interface, σ_x. The governing equation for this flow can be written as

$$\frac{d}{dy}\left(\mu\frac{du}{dy}\right) + \sigma_x\delta(y) = 0 \tag{2.9}$$

where u is the x component of the velocity. The solution of Equation (2.9) is subject to the no-slip boundary condition on the walls and because of symmetry zero velocity gradient at the symmetry axis. At each interface, the jump in shear stresses is balanced by the surface tension forces. The solution to Equation (2.9) can easily be found as

$$u(y) = \begin{cases} 2\sigma_x d/\mu_o(1 - |y|/d) & \text{if } d/2 < |y| < d \\ \sigma_x d/\mu_o & \text{if } |y| < d/2 \end{cases}$$

By integrating the velocity across the channel, the total mass flux is

$$Q_{ex} = \frac{3}{4}\frac{\sigma_x d^2}{\mu_o}$$

We examine the convergence of Q by computing the total mass flux at different resolution when the flow becomes fully developed, reaching a steady state. Figure 2.13 shows the mass flux normalized by the exact mass flux for different mesh

size. The test is done on 1×1 domain with 16×16 grid points, 32×32 grid points, 64×64 grid points and 128×128 grid points. As we increase the resolution, or decrease the mesh size, it is seen that the solution converges well to the exact solution. This further establishes the correctness and the accuracy of the method.

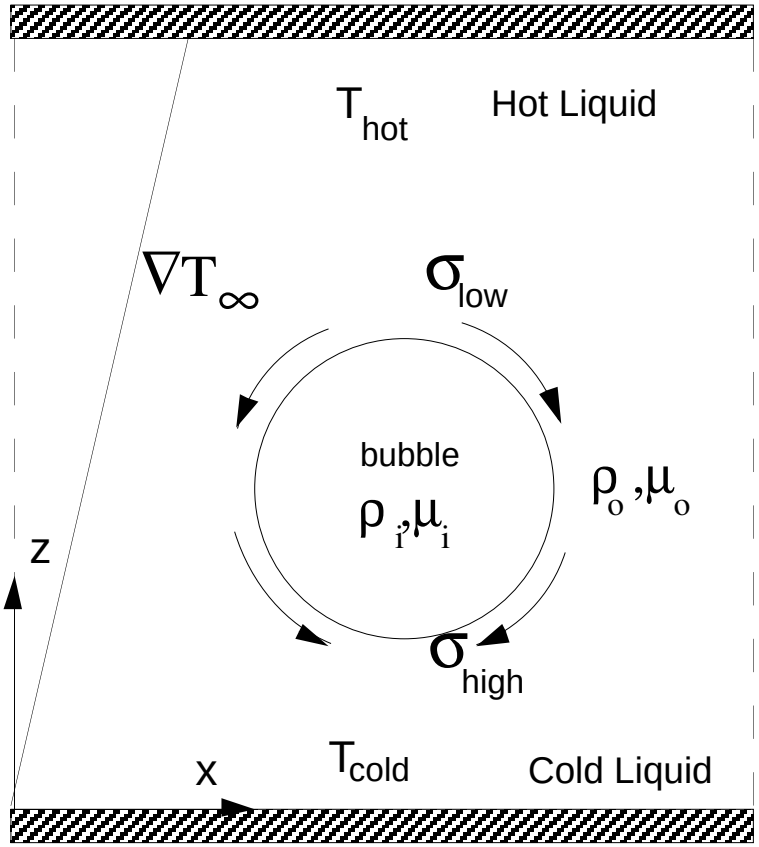

Figure 2.1: The computational setup. The top and bottom wall are no-slip boundaries with constant temperature T_{hot} and T_{cold}. The horizontal boundaries are periodic

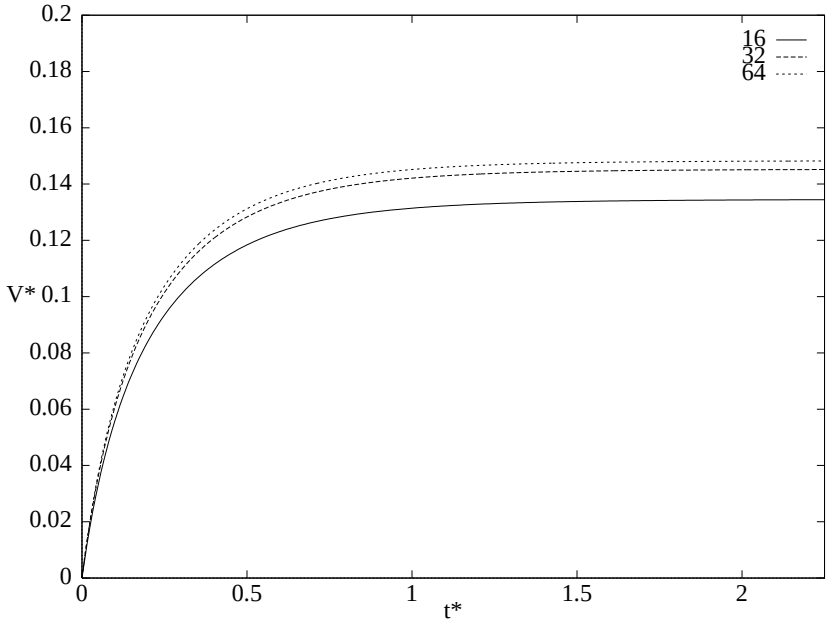

Figure 2.2: Velocity versus time. Convergent test for a single two-dimensional bubble on a computational domain which is 4 bubble radii in each direction.

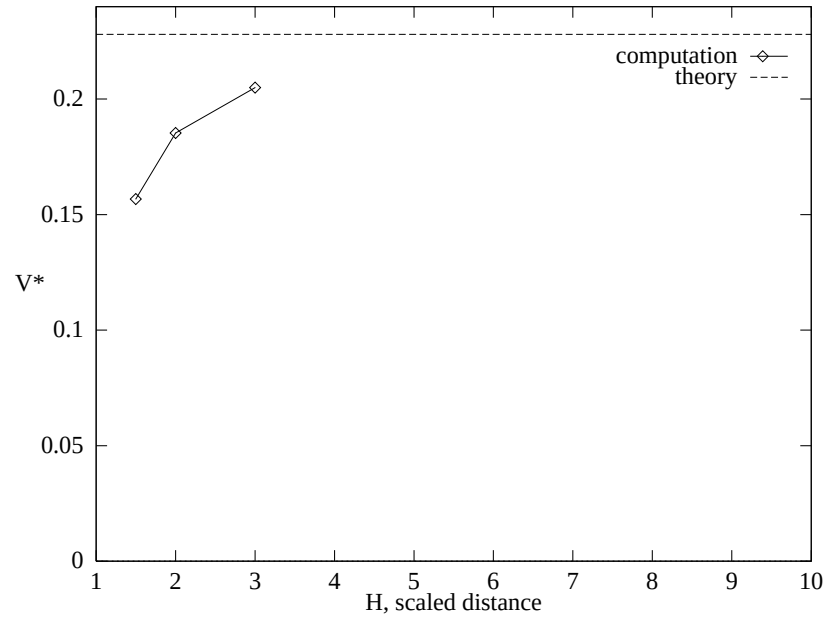

Figure 2.3: Velocity versus box size for a single bubble in 3d. The resolution is 48^3 grid points, 64^3 grid points and $80^2 \times 96$ grid points, respectively.

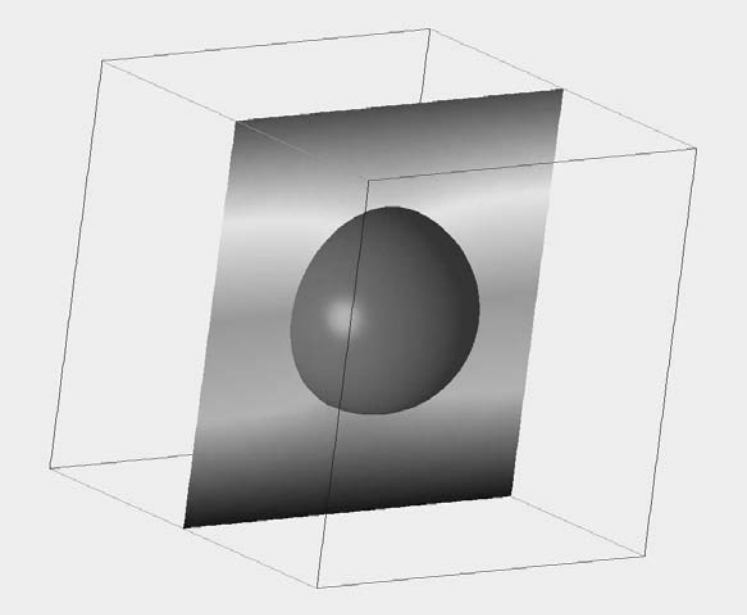

Figure 2.4: The temperature field in the middle plane of the computational domain. The domain is four bubble radii in each direction. The bottom wall is cold and the top wall is hot.

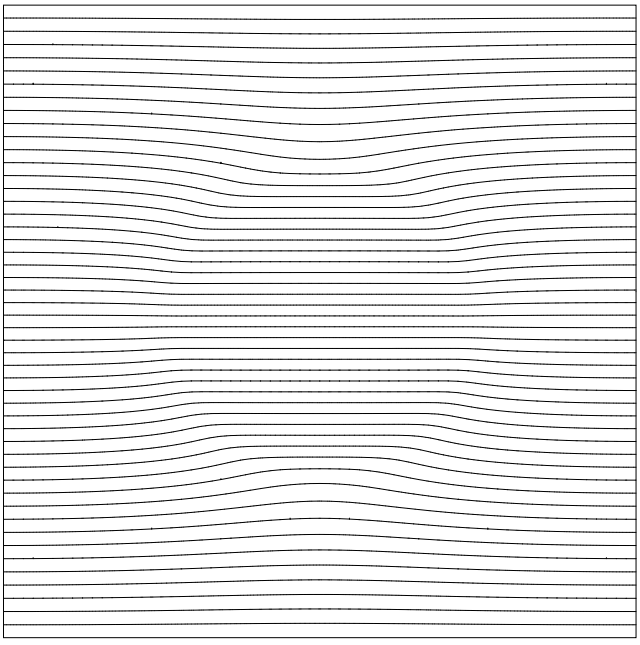

Figure 2.5: Temperature contours in the middle plane of the computational domain. 50 equally spaced contours are shown.

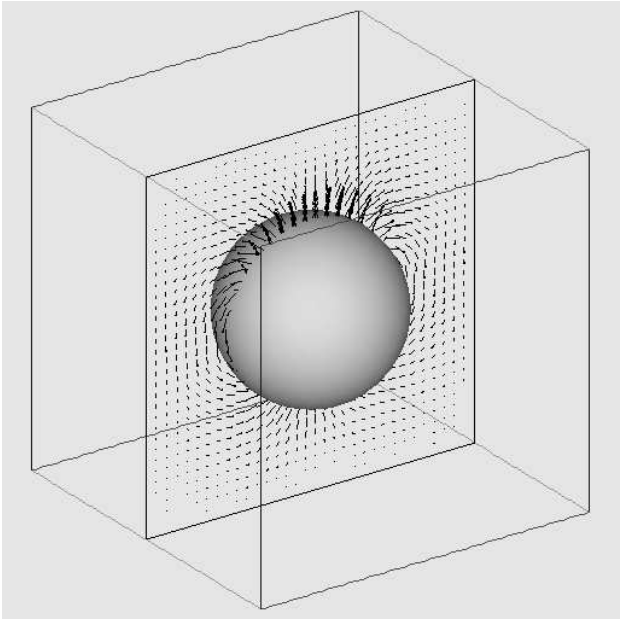

Figure 2.6: The velocity field in the middle plane of the computational domain.

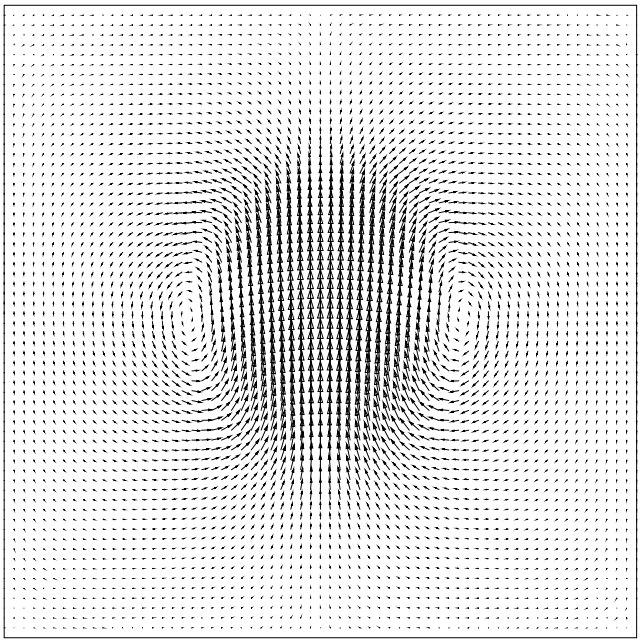

Figure 2.7: Details of the velocity field in the middle plane of the computational domain.

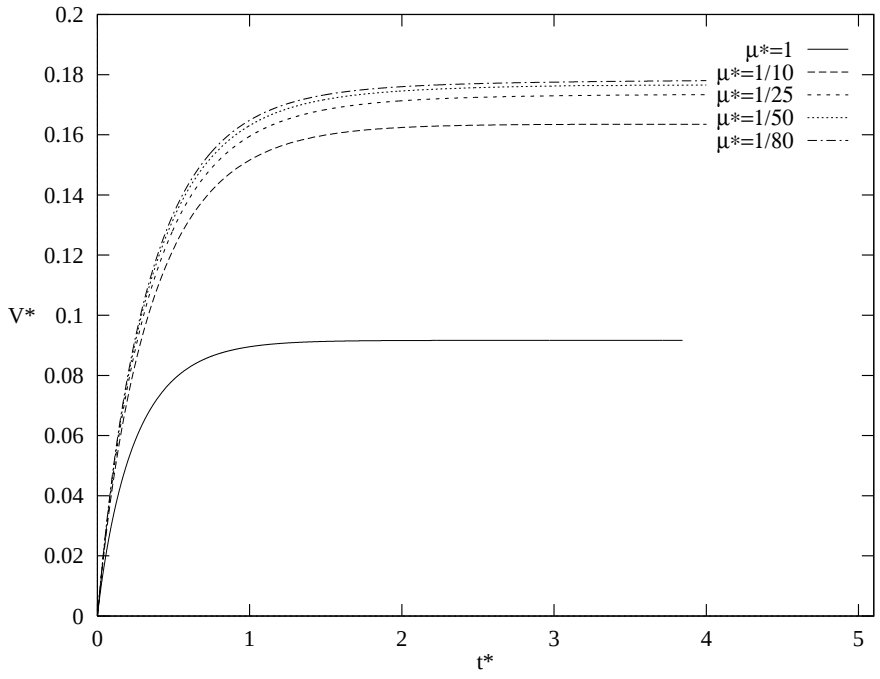

Figure 2.8: Effect of the viscosity ratio on the migration velocity.

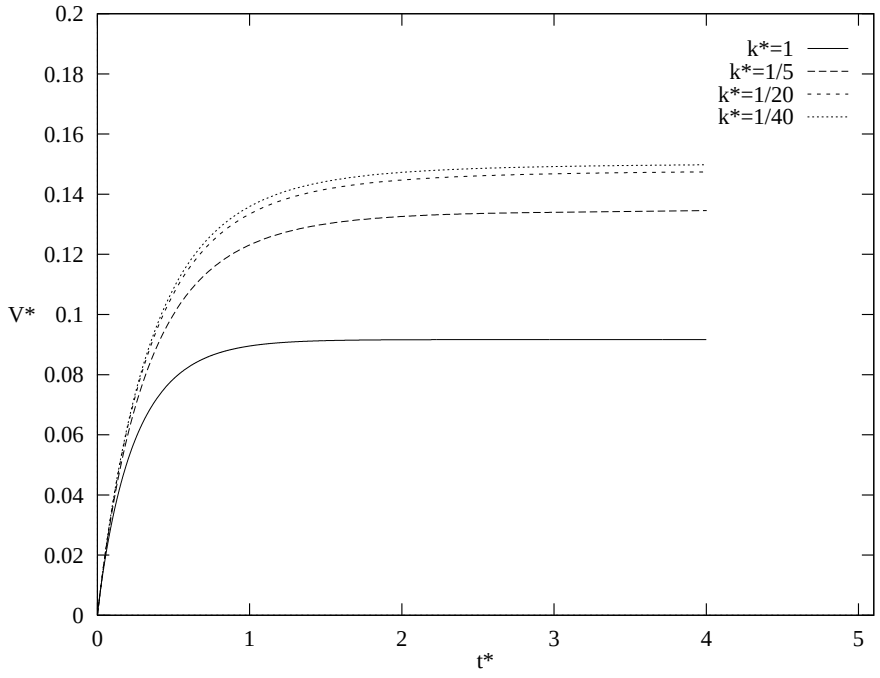

Figure 2.9: Effect of the conductivity ratio on the migration velocity.

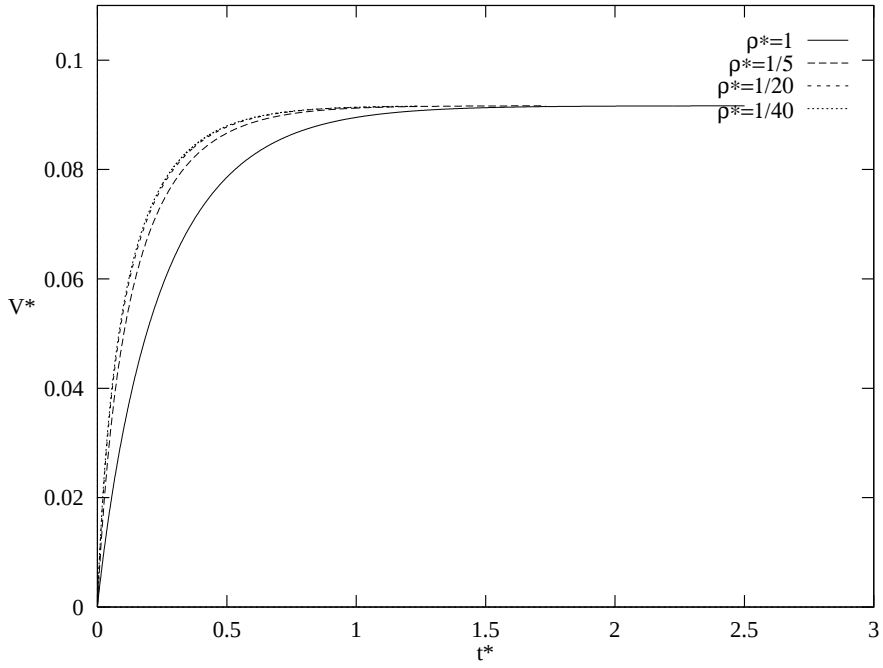

Figure 2.10: Effect of the density ratio on the migration velocity.

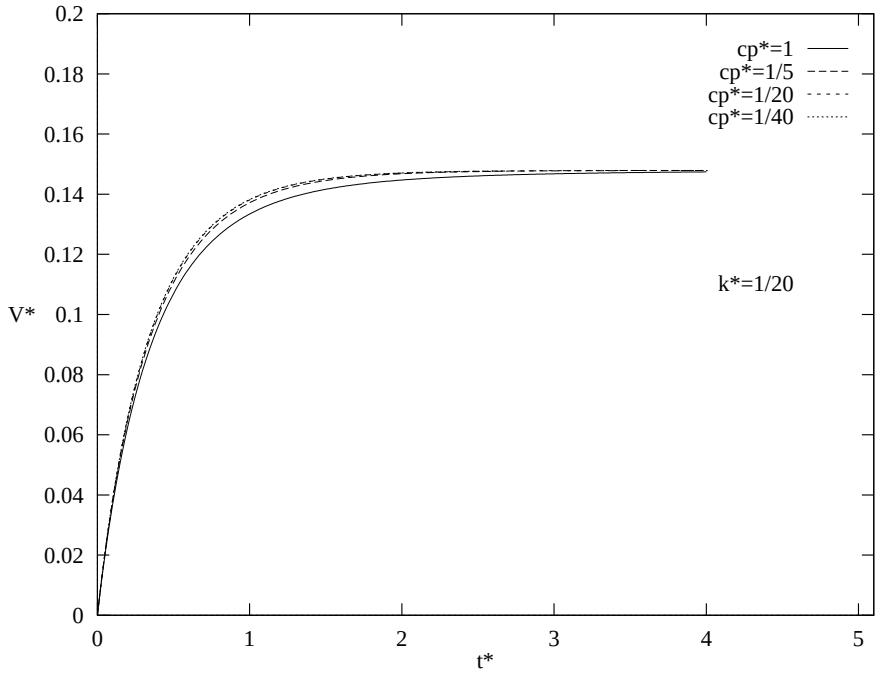

Figure 2.11: Effect of the heat capacity ratio on the migration velocity.

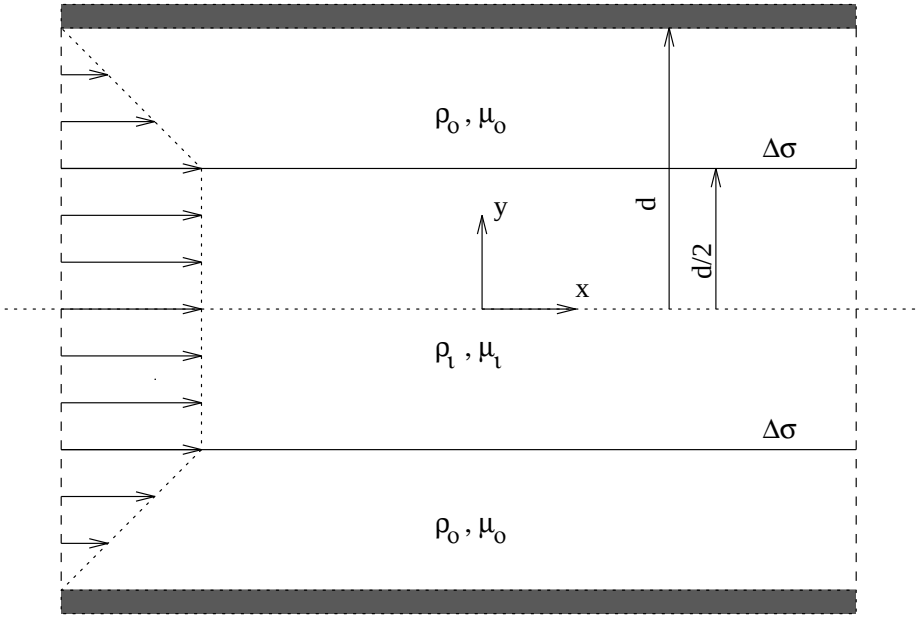

Figure 2.12: Schematic of the third test problem.

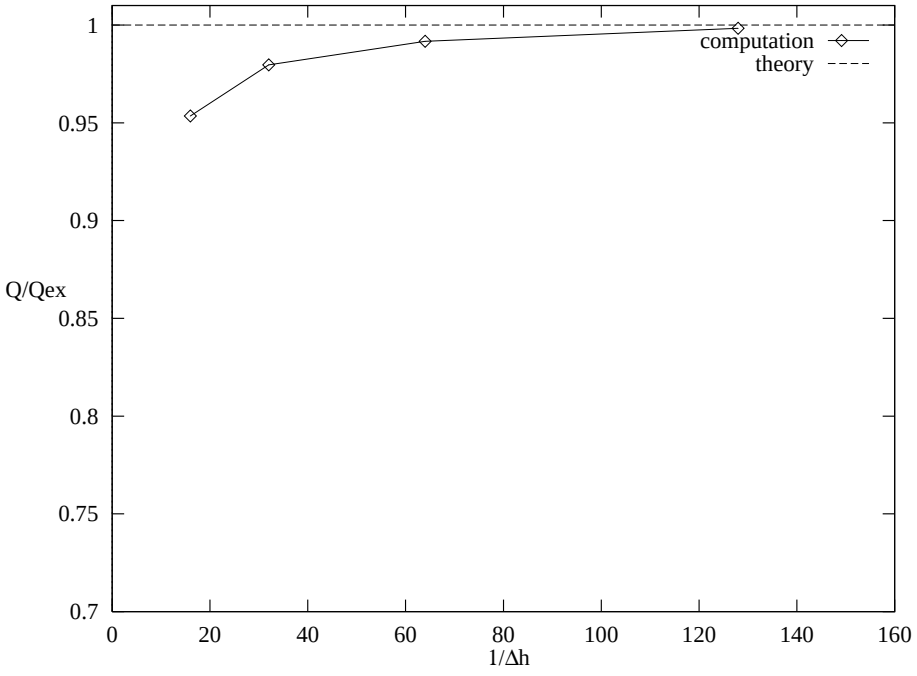

Figure 2.13: Resolution test for the problem in Figure 2.12. Total mass flux scaled by the exact mass flux versus grid resolution.